Infrared Optical Properties of Ferropericlase ($Mg_{1-x}Fe_xO$): Experiment and Theory

Tao Sun,[1, *] Philip B. Allen,[1] David G. Stahnke,[2]

Steven D. Jacobsen,[3] and Christopher C. Homes[4]

[1]*Department of Physics and Astronomy,*

State University of New York, Stony Brook, New York 11794

[2]*Department of Physics, University of California, San Diego, La Jolla, CA 92093*

[3]*Department of Earth and Planetary Sciences,*

Northwestern University, Evanston, IL 60208

[4]*Condensed Matter Physics & Materials Science Department,*

Brookhaven National Laboratory, Upton, New York 11973

(Dated: February 1, 2008)

Abstract

The temperature dependence of the reflectance spectra of magnesium oxide (MgO) and ferropericlase ($Mg_{1-x}Fe_xO$, for $x = 0.06$ and $x = 0.27$) have been measured over a wide frequency range (≈ 50 to $32\,000$ cm^{-1}) at 295 and 6 K. The complex dielectric function has been determined from a Kramers-Kronig analysis of the reflectance. The spectra of the doped materials resembles pure MgO in the infrared region, but with much broader resonances. We use a shell model to calculate the dielectric function of ferropericlase, including both anharmonic phonon-phonon interactions and disorder scattering. These data are relevant to understanding the heat conductivity of ferropericlase in the earth's lower mantle.

PACS numbers: 63.20.Kr, 63.20.Mt, 74.25.Kc, 78.30.-j

I. INTRODUCTION

Ferropericlase, ($Mg_{1-x}Fe_xO$, with $x = 0.10$-0.15), is thought to be one of the major constituents of the earth's lower mantle (660-2900 km depth).[1] The name 'magnesiowüstite' is also used, but properly refers to the doping region x close to the wüstite (x=1), rather than the periclase (x=0) limit. Transport properties of (Mg,Fe)O are therefore important in modeling the Earth's thermal state and evolution, where both conduction and convection are operative.[2,3] The two heat carriers in conduction for an insulating mineral like ferropericlase are phonons and photons. Phonons (extended or localized) are distributed in the far and mid-infrared frequency range. They can be scattered by various defects (e.g. impurities, grain boundaries, . . .) and by the intrinsic anharmonic phonon-phonon interactions. Photons are described by Planck's black-body radiation formula, reaching energies ~ 1 eV at 2000-3000 K. The photon-matter interaction is more complex. Far- and mid-infrared photons usually couple with infrared-active vibrations. Photons of higher frequency can induce pure electronic transitions or vibronic transitions, depending on the details of the system's electronic states and adiabatic potential-energy surfaces. Goncharov et $al.$[4] measured the optical absorption spectra of $Mg_{1-x}Fe_xO$ (with x=0.06, 0.15, and 0.25) across the high-spin/low-spin transition,[5,6,7] which occurs over a pressure range of 40-60 GPa at room temperature. Their results indicate that low-spin (Mg,Fe)O will exhibit lower (rather than higher[8]) radiative heat conductivity than high-spin phase due to the red-shift of the charge-transfer edge. The origin of this spin transition and its influence on the radiative heat conductivity of ferropericlase are further investigated recently.[9] A complete picture of the thermal conductivity must include contributions from both phonons and photons.

As a solid solution, ferropericlase has a vibrational frequency spectrum similar to that of pure MgO. However, with strong disorder scattering of propagating vibrational states, the harmonic eigenstates of the disordered crystal do not necessarily have a well defined wave number, and may not propagate ballistically. In addition, the anharmonic phonon-phonon interactions causes a shoulder at $\sim 640\,\mathrm{cm^{-1}}$ in the infrared (IR) reflectance spectrum of pure MgO.[10] Thus anharmonicity should also be included in analyzing the infrared reflectance of ferropericlase.

In this paper we report the temperature-dependent infrared reflectance measurements of magnesium oxide and ferropericlase for several Fe concentrations at ambient pressure. We

construct a model in which anharmonic phonon-phonon interactions and disorder scattering are treated separately. Their effects are then combined for comparison with the experimental data.

II. EXPERIMENTAL MEASUREMENTS

The samples we examined are homogeneously doped single crystals, in which $Fe^{3+}/\sum Fe \approx 0.02$ for the 6% sample and 0.05 for the 27% sample. However, in our analysis the influence of Fe^{3+} and magnesium vacancies is ignored. A detailed description on the samples' synthesis, crystallography and elastic properties is in Ref. 11. The samples are rectangular slabs with typical dimensions of $1\,\text{mm} \times 2\,\text{mm}$, with a thickness of ≈ 0.3 mm. In order to reduce interference effects due to reflections from the back surface, the samples have been wedged. However, due to the thin nature of the samples, the largest wedge that could be introduced was $\simeq 15°$. The reflectance spectra has been measured at a near-normal angle of incidence at 295 and 6 K over a wide frequency range from ≈ 50 to about $32\,000$ cm^{-1} on Bruker IFS 66v/S and 113v spectrometers using an *in-situ* evaporation technique.[12] The measured reflectance at 295 and 6 K of pure MgO, and $Mg_{1-x}Fe_xO$, for $x = 0.06$ and $x = 0.27$ are shown in Figs. 1(a), (b) and (c), respectively. Although wedging the samples has been very effective at reducing interference effects, weak fringes may still be detected at low temperature below about 150 cm^{-1}. The complex dielectric function $\epsilon = \epsilon_1 + i\epsilon_2$ has been determined from a Kramers-Kronig analysis of the reflectance, where extrapolations are supplied for $\omega \to 0, \infty$. At low frequency, an insulating response is assumed and $R(\omega \to 0) \simeq 0.27$, 0.28 and 0.31 for MgO, and the 6% and 27% Fe-doped materials, respectively. Above the highest measured frequency the reflectance has been assumed to be constant to approximately $75\,000$ cm^{-1}, above which a free-electron approximation has been assumed ($R \propto 1/\omega^4$). The imaginary part of the resulting dielectric function at 6 and 295 K of pure MgO, and $Mg_{1-x}Fe_xO$, for $x = 0.06$ and $x = 0.27$, are shown in Figs. 1(d), (e) and (f), respectively. The imaginary part of the dielectric function contains most of the physical information, and is the focus of our theoretical analysis. The optical features have been fit to a classical oscillator model using the complex dielectric function

$$\epsilon(\omega) = \epsilon_\infty + \sum_j \frac{\omega_{p,j}^2}{\omega_{\text{TO},j}^2 - \omega^2 - i2\omega\gamma_j}, \tag{1}$$
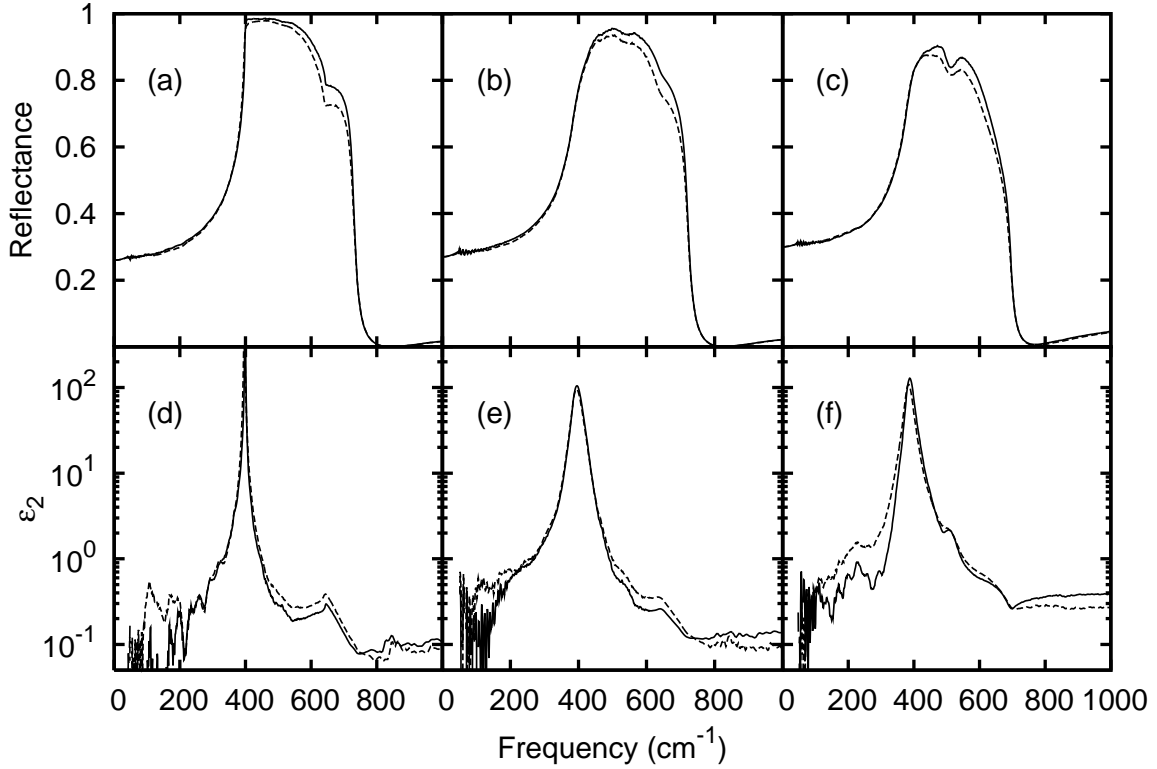
3

FIG. 1: The measured reflectance $R(\omega)$; (a) pure MgO, and $Mg_{1-x}Fe_xO$ for (b) 6% and (c) 27% Fe-doping. The corresponding imaginary part of the dielectric functions $\epsilon_2(\omega)$; (d) pure MgO, and $Mg_{1-x}Fe_xO$ for (e) 6% and (f) 27% Fe-doping. The solid line corresponds to data measured at 6 K, dashed line corresponds to data at 295 K.

where ϵ_∞ is a high-frequency contribution, and $\omega_{TO,j}$, $2\gamma_j$ and $\omega_{p,j}$ are the frequency, full width and effective plasma frequency of the jth vibration. The results of non-linear least-squares fits to the reflectance and $\epsilon_2(\omega)$ are shown in Table I. In addition to the strong feature in $\epsilon_2(\omega)$ seen at about 400 cm^{-1}, other features at $\approx$ 520 and $\approx$ 640 cm^{-1} are also clearly visible in $\epsilon_2(\omega)$ shown in Fig. 1; however, these features are very weak and as a result the the strengths and widths of these modes are difficult to determine reliably.

TABLE I: A comparison of the fitted values of the static and high-frequency contributions to the real part of the dielectric function at room temperature, as well as the fitted frequency, full width and effective plasma frequency (ω_{TO}, 2γ and ω_p, respectively) of the feature associated with the strong TO mode in MgO, and the 6% and 27% Fe-doped materials at 295 and 6 K. The units of ω_{TO}, 2γ and ω_p are in cm^{-1}. The strength of the TO mode is also expressed as a dimensionless oscillator strength $S = \omega_p^2/\omega_{\text{TO}}^2$.

			295 K			6 K		
$\text{Mg}_{1-x}\text{Fe}_x\text{O}$	ϵ_0^a	ϵ_∞^a	ω_{TO}^b	$2\gamma^c$	ω_p^d (S)	ω_{TO}^b	$2\gamma^c$	ω_p^d (S)
pure	9.2	2.95	396.5	3.44	1010 (6.5)	398.9	1.72	1030 (6.7)
$x = 0.06$	10.8	3.10	395.6	30.5	1090 (7.6)	396.7	29.1	1120 (8.0)
$x = 0.27$	11.8	3.65	384.5	28.6	1100 (8.2)	388.6	25.7	1140 (8.6)

^{a}Values at 295 K, the estimated uncertainty is about ±0.1.
^{b}The uncertainty in ω_{TO} is ±0.1 cm^{-1}.
^{c}The uncertainties for 2γ are ±0.1 cm^{-1} in the pure material, and ±0.5 cm^{-1} in the Fe-doped materials.
^{d}The uncertainty in ω_p is ±20 cm^{-1}.

III.   COMPUTATIONAL METHODS

A.   General Scheme

Infrared dielectric properties of ionic crystals are contained in the linear response function $\epsilon_{\alpha\beta}(\omega) = \epsilon_{\alpha\beta}(\infty) + 4\pi\chi_{\alpha\beta}(\omega)$.[13] Considering only the first-order moment of the electric dipole, the dielectric susceptibility of a crystal can be related to its displacement-displacement retarded Green's function by:

$$
\begin{aligned}
\chi_{\alpha\beta}(\omega) &= -\frac{1}{NV_c} \int_{-\infty}^{+\infty} \frac{\theta(t-t')}{i\hbar} \langle [D_\alpha(t), D_\beta(t')] \rangle e^{i\omega(t-t')} \, d(t-t') \\
&= -\frac{1}{NV_c} \sum_{ls\gamma} \sum_{l's'\delta} Z_{\alpha\gamma}(ls) Z_{\beta\delta}(l's') \int_{-\infty}^{+\infty} \frac{\theta(t-t')}{i\hbar} \langle [u_\gamma(ls;t), u_\delta(l's';t')] \rangle e^{i\omega(t-t')} \, d(t-t') \\
&= -\frac{1}{NV_c} \sum_{ls\gamma} \sum_{l's'\delta} Z_{\alpha\gamma}(ls) Z_{\beta\delta}(l's') G_{\gamma\delta}(ls, l's'; \omega),
\end{aligned}
\tag{2}
$$

where $D_\alpha(t) = \sum_{ls\beta} Z_{\alpha\beta}(ls) u_\beta(ls;t)$ is the α component of the first order electric dipole of the whole crystal, $Z_{\alpha\beta}(ls)$ is the Born effective charge tensor of the atom s at site l, and

$u_\beta(ls; t)$ is the atom's displacement at time t. The volume of a single cell is V_c, and N is the number of the cells in the whole crystal. The Green's function $G_{\alpha\beta}(ls, l's'; t - t')$ is defined as:

$$G_{\alpha\beta}(ls, l's'; t - t') = \frac{\theta(t - t')}{i\hbar}\langle[u_\alpha(ls; t), u_\beta(l's'; t')]\rangle, \tag{3}$$

which can be evaluated from its equation of motion.[14] For a harmonic crystal, the vibrational Hamiltonian is quadratic and can be solved exactly. We denote the eigenvectors of a pure crystal as $\frac{1}{\sqrt{N}}\hat{e}_\alpha(s|\mathbf{q}j)e^{i\mathbf{q}\cdot\mathbf{R}(ls)}$, the corresponding eigenvalues as $\omega_{\mathbf{q}j}$, those of a disordered crystal as $e_\alpha(s|j)$ and ω_j, the Green's function of the pure as $\mathbf{g}$, the disordered as $\mathbf{G}^0$. Then

$$g_{\alpha\beta}(ls, l's'; \omega) = \sum_{\mathbf{q}j} \frac{\hat{e}_\alpha(s|\mathbf{q}j)\hat{e}_\beta^*(s'|\mathbf{q}j)e^{i\mathbf{q}\cdot(\mathbf{R}(ls) - \mathbf{R}(l's'))}}{N\sqrt{M(s)M(s')}(\omega^2 - \omega_{\mathbf{q}j}^2 + i2\omega\eta)}, \tag{4}$$

$$G_{\alpha\beta}^0(ls, l's'; \omega) = \sum_{j} \frac{e_\alpha(ls|j)e_\beta^*(l's'|j)}{\sqrt{M(ls)M(l's')}(\omega^2 - \omega_j^2 + i2\omega\eta)}, \tag{5}$$

where the mass of the atom s is denoted as $M(s)$ in the pure crystal, $M(ls)$ in the disordered crystal, with the extra label l to specify its site, η is an infinitesimal number ensuring causality.

Anharmonic interaction will couple these modes and make exact solution impossible. The standard treatment of this many-body effect uses the Dyson equation to define a self-energy for each mode. We can either choose $e_\alpha(s|j)$ as the unperturbed states, then the only interaction will be anharmonicity, or choose $\frac{1}{\sqrt{N}}\hat{e}_\alpha(s|\mathbf{q}j)e^{i\mathbf{q}\cdot\mathbf{R}(ls)}$ as the basis and treat disorder as an extra perturbation. The first approach has been used by one of the authors (PBA) to study the anharmonic decay of vibrational states in amorphous silicon.[15] In this paper we use a hybrid approach. We write the dielectric function of a disordered anharmonic crystal in the perfect crystal harmonic basis as

$$\begin{aligned}
\epsilon_{\alpha\beta}(\omega) &= \epsilon_{\alpha\beta}(\infty) + 4\pi\chi_{\alpha\beta}(\omega) \\
&= \epsilon_{\alpha\beta}(\infty) + \frac{4\pi}{V_c}\sum_{j=1}^{\text{TO}} \frac{\sum_{s\gamma} Z_{\alpha\gamma}(s)\frac{\hat{e}_\gamma(s|0j)}{\sqrt{M(s)}} \sum_{s'\delta} Z_{\beta\delta}(s')\frac{\hat{e}_\delta^*(s'|0j)}{\sqrt{M(s')}}}{\{\omega(0j)^2 - \omega^2 + 2\omega(0j)(\Delta(0j,\omega) - i\Gamma(0j,\omega))\}},
\end{aligned} \tag{6}$$

where $\omega(0j) \equiv \omega_{\text{TO},j}$ is the frequency at $\mathbf{q} = 0$ of the jth TO branch. The terms $\Delta(0j,\omega)$ and $\Gamma(0j,\omega)$ correspond to the real and imaginary part of the mode's self-energy $\Sigma(0j,\omega)$. Then we split this self-energy into two parts: $\Sigma = \Sigma_{\text{anharm}} + \Sigma_{\text{disorder}}$. Each piece is calculated independently. This is equivalent to omitting all the diagrams where the disorder

scattering vertex appears inside an anharmonic interaction loop. The anharmonic interaction of ferropericlase is assumed to be the same as that of pure MgO, i.e. the influence of disorder on anharmonic coefficients is totally ignored. Disorder is treated by exact diagonalization without anharmonicity, it is then converted to a self-energy of the TO mode in the perfect crystal harmonic basis. These approximations are tested by comparing with the experimental results.

B.   Shell Model

The scheme described above is general. It does not depend on which microscopic model is chosen to get harmonic phonons, disorder scattering strength, and higher-order force constants. Here we use an anharmonic shell model, with shell parameters fitted to experiments. The harmonic phonon properties in this paper are calculated with the general utility lattice program (GULP) code.[16]

Two sets of shell parameters[16,17] are used for MgO: S-I and B, and one for FeO: S-II. S-I and S-II are rigid shell models in which O^{2-} has the same set of parameters, thus they can be conveniently used to simulate ferropericlase. B is an isotropic breathing shell model which gives better fit to the experimental data. However, it can not be directly used for ferropericlase. For FeO the elastic constants $C_{12} > C_{44}$, while the isotropic breathing shell model is only suitable for cases where $C_{12} < C_{44}$.[18] We treat B as a reference to check our anharmonic calculations based on S-I. All the model parameters are listed in Table II. Table III contains the calculated physical properties and corresponding experimental values. Phonon dispersion curves for the pure crystals of MgO and FeO are shown in Fig. 2.

C.   Anharmonicity

A complete calculation of anharmonicity is tedious, even for a pure crystal.[13] Thus we ignore the less important terms and focus on the dominant one. From Eq. (6) it is clear that since $|\Sigma| = |\Delta - i\Gamma|$ is small compared to ω_{TO}, the real part of the self-energy Δ has negligible influence on $\epsilon_2(\omega)$, except to shift its resonant frequency. The shell models we use are fitted to the experimental data measured at room temperature. The anharmonic shift is small, compared with the shift caused by impurity scattering. Thus, we ignore it completely

TABLE II: Shell model parameters used in the calculation.[16,17] The short-range repulsive potential is assumed to be a two-body Buckingham type: for S-I and S-II, $V(r) = A \exp(-r/\rho) - C/r^6$; for B, $V(r) = A \exp(-(r - r_0)/\rho) - C/r^6$. The parameter k represents the spring constant between core and shell. Rows in which atomic symbols have a star (*) are for the B model. The label 'shell' denotes a potential that acts on the central position of the shell, while 'bshell' denotes an interaction that acts on the radius of the shell which was fixed at 1.2 Å. An extra parameter in B model is $k_{BSM} = 351.439$ eVÅ^{-2}. The equilibrium shell radius r_0 is 1.1315 Å after optimization.

	Z_{core} (e)	Z_{shell} (e)	k (eV)
O	0.9345	−2.9345	51.712
Mg	2	–	–
Fe	−1.1682	3.1682	69.562
O*	0.8	−2.8	46.1524
Mg*	2	–	–

	A (eV)	ρ (Å)	C (eV·Å^6)
O shell-O shell	22764.3	0.149	20.37
Mg core-O shell	1346.6	0.2984	0.0
Fe shell-O shell	1231.2	0.3086	0.0
O* shell-O* shell	0.0	0.3	54.038
Mg* core-O* bshell	28.7374	0.3092	0.0

TABLE III: Physical properties of pure MgO and FeO, compared with shell model results.

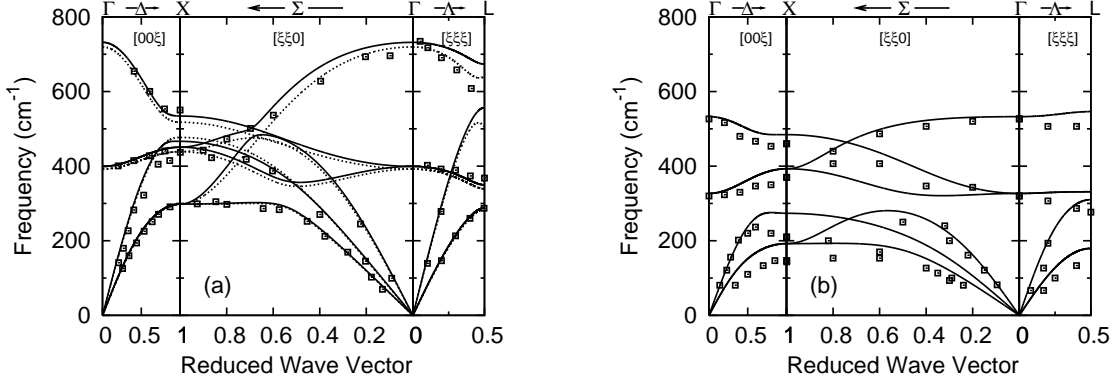|	a (Å)	C_{11} (GPa)	C_{12} (GPa)	C_{44} (GPa)	ϵ_0	ϵ_∞	TO (cm^{-1})
MgO (exp[16,17,21])	4.212	297.0	95.2	155.7	9.86	2.96	401
S-I	4.225	370.9	163.0	163.0	9.88	2.94	399
B	4.212	297.0	95.0	155.7	9.89	2.94	392
FeO (exp[21])	4.310	359	156	56	14.2	5.4	320
S-II	4.324	327	149	149	14.18	5.34	327

FIG. 2: Phonon dispersions of the pure crystals. (a) MgO, solid line corresponds to the rigid-shell model S-I, dashed line to the isotropic breathing-shell model B, dots are the experimental data taken from Ref. 19; (b) FeO, solid line corresponds to the rigid-shell model S-II, dots are the experimental data taken from Ref. 20.

and only consider the imaginary part of the self energy $\Gamma_{\text{anharm}}(0j, \omega)$. To the lowest order $\Gamma_{\text{anharm}}(0j, \omega)$ can be written as[13]

$$\Gamma_{\text{anharm}}(0j, \omega) = \frac{18\pi}{\hbar^2} \sum_{\mathbf{q}j_1j_2} \left| V \begin{pmatrix} 0 & \mathbf{q} & -\mathbf{q} \\ j & j_1 & j_2 \end{pmatrix} \right|^2 \{(n_1 + n_2 + 1)[\delta(\omega_1 + \omega_2 - \omega) - \delta(\omega_1 + \omega_2 + \omega)]$$
$$+ (n_2 - n_1)[\delta(\omega_2 - \omega_1 + \omega) - \delta(\omega_1 - \omega_2 + \omega)]\}, \tag{7}$$

where $n_1 = n(\mathbf{q}j_1)$ is the Bose-Einstein population factor of the mode, and $\omega_1 = \omega(\mathbf{q}j_1)$ is the corresponding frequency. The anharmonic coefficient $V \begin{pmatrix} 0 & \mathbf{q} & -\mathbf{q} \\ j & j_1 & j_2 \end{pmatrix}$ is

$$V \begin{pmatrix} 0 & \mathbf{q} & -\mathbf{q} \\ j & j_1 & j_2 \end{pmatrix} = \frac{1}{3!} \sum_{\alpha\beta\gamma} \sum_{s_1s_2s_3} \sum_{l_2l_3} \Phi_{\alpha\beta\gamma} \begin{pmatrix} 0 & l_2 & l_3 \\ s_1 & s_2 & s_3 \end{pmatrix} \hat{e}_\alpha(s_1|0j)\hat{e}_\beta(s_2|\mathbf{q}j_1)\hat{e}_\gamma(s_3|-\mathbf{q}j_2)$$
$$\left(\frac{\hbar^3}{8\omega(0j)\omega(\mathbf{q}j_1)\omega(-\mathbf{q}j_2)M(s_1)M(s_2)M(s_3)} \right)^{\frac{1}{2}} \exp\{i\mathbf{q} \cdot [\mathbf{R}(l_2s_2) - \mathbf{R}(l_3s_3)]\}. \tag{8}$$

The third-order force constants $\Phi_{\alpha\beta\gamma} \begin{pmatrix} 0 & l_2 & l_3 \\ s_1 & s_2 & s_3 \end{pmatrix}$ are large only for the nearest neighbors. Symmetry will restrict most of them to be zero, and among those nonzero terms only two are independent. The general formula for third order force constants is[13]

$$\Phi_{\alpha\beta\gamma} \begin{pmatrix} 0 & 0 & l' \\ s & s & s' \end{pmatrix} = BR_\alpha R_\beta R_\gamma + C(R_\alpha \delta_{\beta\gamma} + R_\beta \delta_{\alpha\gamma} + R_\gamma \delta_{\alpha\beta}),$$
$$B = \frac{\phi'''}{R^3} - \frac{3\phi''}{R^4} + \frac{3\phi'}{R^5},$$
$$C = \frac{\phi''}{R^2} - \frac{\phi'}{R^3}, \tag{9}$$

9

where R is the lattice distance between the ion $\binom{0}{s}$ and $\binom{l'}{s'}$, and R_α is its projection along α direction. The term $\phi(r)$ is the two-body pair potential, and ϕ', ϕ'' ... are derivatives with respect to r. Following E. R. Cowley,[22] we compute $\Phi_{\alpha\beta\gamma}\left(\begin{smallmatrix} 0 & 0 & l' \\ s & s & s' \end{smallmatrix}\right)$ by direct differentiation over the nearest-neighbour short-range potentials and Coulomb potentials. For the rigid-shell model S-I, $\phi(r) = A\exp(-r/\rho) - \frac{4e^2}{r}$. For the breathing-shell model B, $\phi(r) = A\exp(-(r - r_0)/\rho) - \frac{4e^2}{r}$. To be more specific, if we take a Mg^{2+} as the origin and denote it as 1, its nearest neighbor O^{2-} along the [100] direction as 2, then from symmetry we can determine $\Phi_{xxx}(112) = \Phi_{xxx}(121) = -\Phi_{xxx}(122) = \Phi_{yyy}(112) = \cdots$, $\Phi_{xyy}(112) = \Phi_{xzz}(112) = \cdots$. Putting in numbers from Table II we obtain $\Phi_{xxx}(112) = -25.34$ eV/$Å^3$, $\Phi_{xyy}(112) = -1.79$ eV/$Å^3$ for the S-I model, and $\Phi_{xxx}(112) = -24.0$ eV/$Å^3$, $\Phi_{xyy}(112) = -1.78$ eV/$Å^3$ for the B model. If we do not include the Coulomb interaction, these values will be $\Phi_{xxx}(112) = -42.70$ eV/$Å^3$ $\Phi_{xyy}(112) = 6.88$ eV/$Å^3$ for the S-I model, and $\Phi_{xxx}(112) = -41.57$ eV/$Å^3$, $\Phi_{xyy}(112) = 7$ eV/$Å^3$ for the B model. Although $\Phi_{xyy}(112)$ is small compared with $\Phi_{xxx}(112)$, it can still have non-negligible influence on the amplitude of the $\Gamma(0j, \omega)$ near 640 cm^{-1}. Other parameters (Born effective charge tensors, harmonic eigenvectors) are obtained from GULP. The integration over q-space is done with the tetrahedron method, using 1/48 of the Brillouin zone, and averaging over x, y, and z polarizations. We use 3345 q-points, equivalent to 160560 q-points in the whole Brillouin zone.

D. Disorder Scattering

The self-energy of a vibrational mode caused by disorder scattering is defined statistically,[14,23]

$$\langle\langle \mathbf{G^0} \rangle\rangle = \mathbf{g} + \mathbf{g}\mathbf{\Sigma}\langle\langle \mathbf{G^0} \rangle\rangle,$$

where $\langle\langle \mathbf{G^0} \rangle\rangle$ denotes the Green's function averaged over different impurity distributions. We slightly modify this definition by including the Born effective charge. From Eqs. (4) and (5), we define the following equation

$$\left\langle\left\langle \sum_\gamma \sum_\delta Z_{\alpha\gamma}(ls) G^0_{\gamma\delta}(ls, l's'; \omega) Z_{\delta\beta}(l's') \right\rangle\right\rangle = \sum_\gamma \sum_\delta Z_{\alpha\gamma}(s) \tilde{g}_{\gamma\delta}(ls, l's'; \omega) Z_{\delta\beta}(s'), \quad (10)$$

where

$$\tilde{g}_{\gamma\delta}(ls, l's'; \omega) = \sum_{\mathbf{q}j} \frac{\hat{e}_\gamma(s|\mathbf{q}j)\hat{e}^*_\delta(s'|\mathbf{q}j)e^{i\mathbf{q}\cdot(\mathbf{R}(ls)-\mathbf{R}(l's'))}}{N\sqrt{M(s)M(s')}(\omega^2 - \omega^2_{\mathbf{q}j} - i2\omega_{\mathbf{q}j}\Sigma_{disorder}(\mathbf{q}j, \omega))}. \quad (11)$$

10

The self-energy defined in this way guarantees that the dielectric susceptibilities calculated from $\mathbf{G}^0$ and $\tilde{\mathbf{g}}$ are the same. Summing over all sites of the crystal leaves only TO modes on the right hand side of Eq. (10). Thus, once we get the averaged dielectric susceptibility $\langle\langle \chi_{\alpha\beta} \rangle\rangle$ from the exact eigenvectors of the disordered crystal, we can extract the self-energy of its TO phonon.

We expand an orthogonal 8-atom MgO unit cell in each direction by 5 times, which gives a $5 \times 5 \times 5$ super-cell containing 1000 atoms. Then we randomly replace the corresponding number of Mg^{2+} by Fe^{2+}. The shell parameters of Mg^{2+} are from S-I model, those of Fe^{2+} are from S-II model, those of O^{2-} are the same in both models. From Eqs. (2) and (5), for each configuration we have a harmonic susceptibility

$$\chi_{\alpha\beta}(\omega) = \frac{1}{NV_c} \sum_{j=1}^{modes} \frac{\displaystyle\sum_{ls\gamma} Z_{\alpha\gamma}(ls) \frac{e_\gamma(ls|j)}{\sqrt{M(ls)}} \sum_{l's'\delta} Z_{\beta\delta}(l's') \frac{e_\delta^*(l's'|j)}{\sqrt{M(l's')}}}{\omega_j^2 - \omega^2 - i2\omega\eta}. \tag{12}$$

We can choose a small value for η and evaluate Eq. (12) directly (Lorentzian broadening). However, insofar as η is finite, it is equivalent to have each mode j in Eq. (12) an imaginary self-energy (life time) linear in frequency ω. The self-energy of the TO phonon Σ_{disorder} extracted from this approach will depend on frequency linearly. Replacing the factor 2ω by $2\omega_j$ won't help either, as each mode j now has a life time independent of frequency, and Σ_{disorder} will be a constant depending on η when $\omega \to 0$. To avoid such artifacts we use

$$\frac{1}{\omega_j^2 - \omega^2 - i2\omega\eta} = \frac{1}{\omega_j^2 - \omega^2} + \frac{i\pi}{2\omega} \left[\delta(\omega - \omega_j) + \delta(\omega + \omega_j)\right]$$

to separate the real (χ_1) and imaginary part (χ_2) of the dielectric susceptibility. Then we divide the vibrational spectrum into equally sized bins (1 cm^{-1}) and compute χ_2 as a histogram. The real part χ_1 is obtained from χ_2 from the Kramers-Kronig relation. Many such super-cells are built and their ϵ_∞ and χ calculated. We find that 10 configurations are sufficient to give a well converged average. The final ϵ_∞ and χ are assumed to be the averaged values of all configurations. To remove the unphysical spikes caused by the finite size of our super-cells, while keeping the main features unchanged, we further smooth the dielectric susceptibility by averaging over adjacent bins iteratively,

$$\chi_2^{n+1}(j) = \frac{1}{6} \left[\chi_2^n(j-1) + 4\chi_2^n(j) + \chi_2^n(j+1)\right]. \tag{13}$$
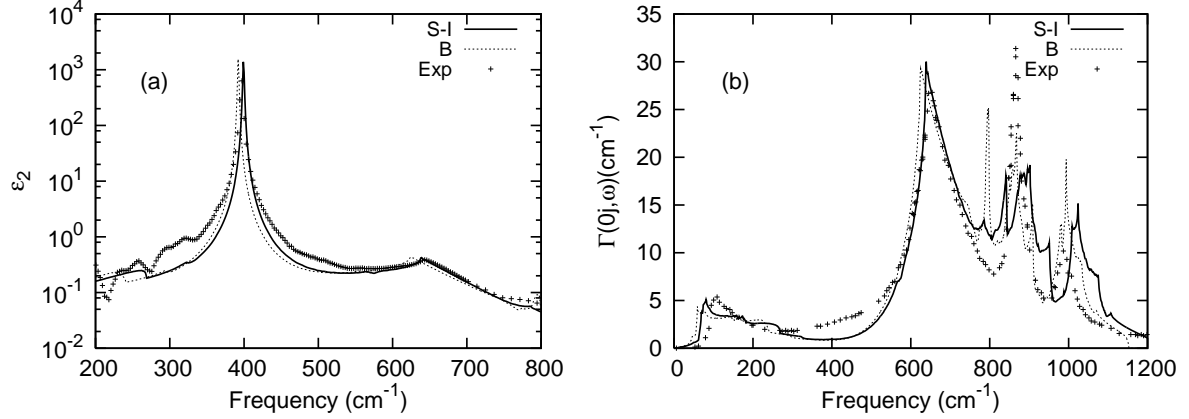
11

FIG. 3: Computed anharmonic properties compared with experimental data for pure MgO. (a) The imaginary part of dielectric function at 295 K; the experimental data are the same as those in Fig. 1(d). (b) The imaginary part of self energy at 295 K; the experimental data are digitized from Ref. 25, which are fit to infared spectra based on a semi-quantum dielectric function model.

In this way we successfully simulate the dielectric function of a 'real' crystal (real in the sense that except for finite size, disorder scattering is treated without any further approximations). These results, together with anharmonicity, are summarized in the next section.

IV.   COMPARISONS AND DISCUSSION

The anharmonic effects in pure MgO are shown in Fig. 3. The computational results and experimental values are quite close, especially near 640 cm^{-1} which corresponds to TO+TA combination mode. It is not surprising, since the procedure we followed was originally developed and worked well for alkali-halide salts, which are similar to MgO. Below 800 cm^{-1}, the rigid shell model S-I and breathing shell model B give almost identical self-energies. The discrepancy in the high-frequency range indicates that the dispersion relations from empirical models are less accurate for high-frequency optical branches. The width of TO mode at the reststrahlen frequency ω_{TO} is less accurate, as $\Gamma_{\text{anharm}}(0j, \omega_{\text{TO}})$ is intrinsically small and higher-order anharmonic effects become important.[24]

Figures 4 and 5 show how anharmonicity and disorder scattering influence the dielectric function. For the 6% sample it is clear that the shoulder near 640 cm^{-1} is caused by anharmonicity, while the shoulder at about 520 cm^{-1} is due to disorder scattering. Disorder scattering becomes stronger for the 27% sample and seems contributes to all the shoulders.
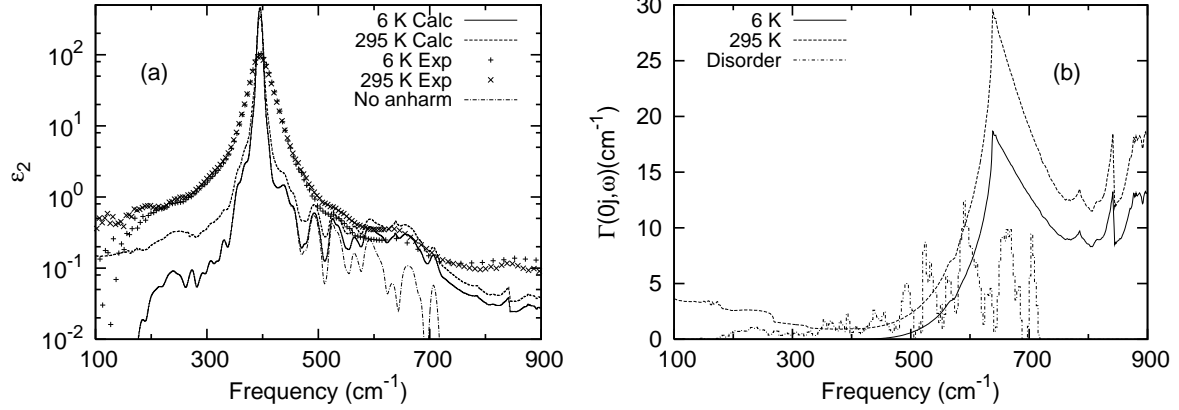
FIG. 4: The anharmonic and disordering scattering effects in $Mg_{1-x}Fe_xO$ for the 6% Fe-doped sample. (a) Imaginary part of the dielectric function. The labels '6 K Calc' and '295 K Calc' denote the calculated curves, including both disorder scattering and anharmonic interactions at the corresponding temperature. Experimental data are the same as those in Fig. 1(e). The label 'No anharm' denotes the dielectric function calculated from disorder scattering only. (b) Imaginary part of self energy. The labels '6 K' and '295 K' denote the self-energies caused by anharmonic interaction at the corresponding temperature; 'disorder' denotes the self-energy due to disorder scattering, which is computed by histogram method where the bin size equals 1 cm^{-1}, then iteratively averaged 30 times. The total self-energies are the sum of these two pieces, and are used in calculating the '6 K Calc' and '295 K Calc' dielectric functions shown in (a).

The shoulder caused by anharmonicity corresponds to a peak in the two-phonon DOS, while shoulders caused by disorder scattering are related to peaks in the one-phonon DOS.

Figure 6 contains the reflectance computed from the dielectric functions at 295 and 6 K shown in Figs. 4 and 5. As in the case of pure MgO, the agreement between theory and experiment is better in the region where the self-energy caused by lowest-order pertubation is large. Near the reststrahlen frequency ω_{TO}, the self-energy is smaller, and $R(\omega)$ is more sensitive to details. Our model underestimates the broadening of the resonance, but correctly identifies the sources of broadening.

It is of interest to determine whether the disorder scattering is mainly due to the differences in mass or in the inter-atomic potential. Thus we repeat the above procedure with a model which only contains mass disorder, i.e. Fe is treated as an isotope of Mg, its shell parameters are the same as Mg^{2+} in S-I model. It turns out the most significant factor
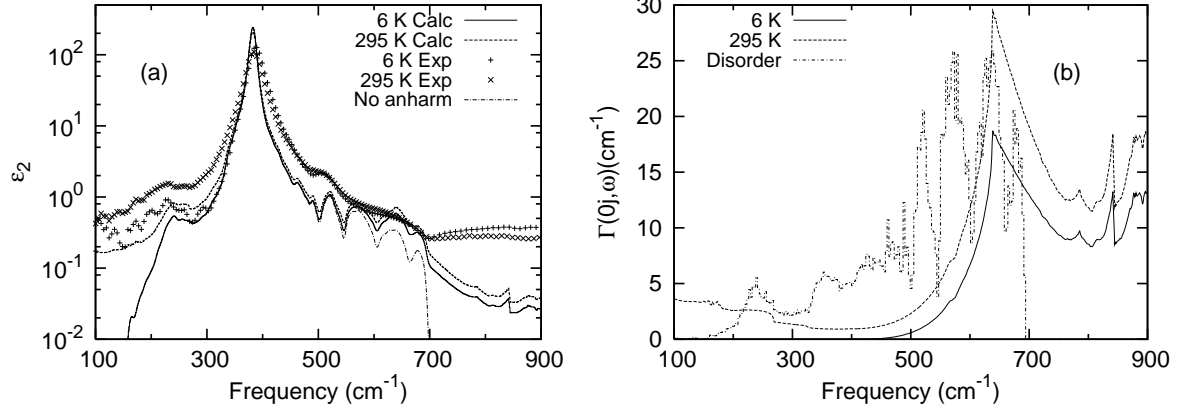
FIG. 5: The anharmonic and disordering scattering effects in $Mg_{1-x}Fe_xO$ for the 27% Fe-doped sample. (a) Imaginary part of the dielectric function; (b) Imaginary part of self energy. The computation procedure is the same as for the 6% Fe doping.
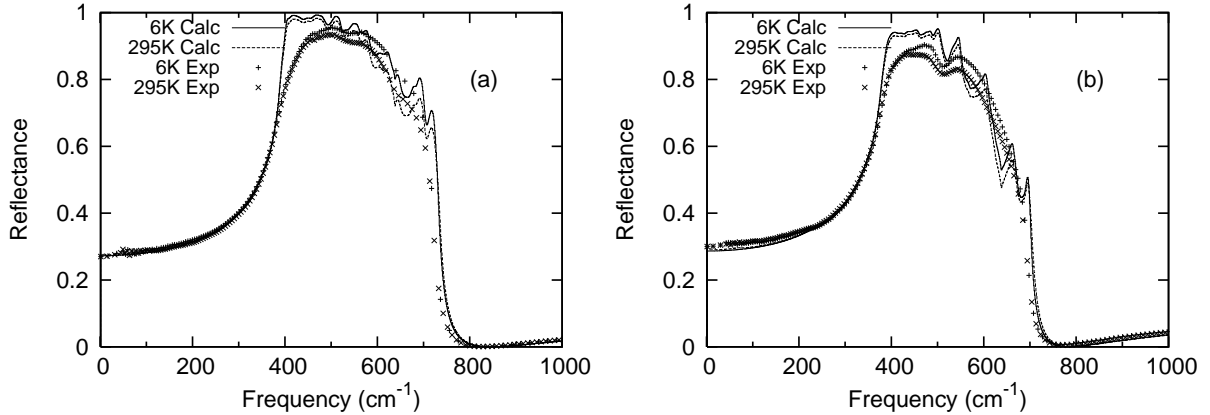

FIG. 6: The calculated infrared reflectance, compared with the experimental data (same as in Fig. 1(b) and (c)) for $Mg_{1-x}Fe_xO$. (a) 6% Fe doping; (b) 27% Fe doping.

is ϵ_∞: For the isotope model (S-I) ϵ_∞ is the same as pure MgO (2.94), for S-II model ϵ_∞ increases to 3.05 for 6% Fe and 3.47 for 27%, in reasonable agreement with the results shown in Table I. Thus the LO frequency predicted from the isotope model is larger than the experimental value. The differences in the inter-atomic potentials change the relative strength of the self-energy, but in both cases the self-energy spectra carry features of the one phonon DOS of pure MgO.

In addition to phonons, electronic transitions may also influence the infrared dielectric properties of ferropericlase. Wong[26] measured the far-infrared absorption spectra of iron-doped MgO. A line at 105 cm^{-1} was observed with a peak absorption coefficient of 1.5 cm^{-1}

14

and a width of $\simeq 9$ cm^{-1} at 20 K in a sample with 0.2% Fe. This feature is attributed to the transition $\Gamma_{5g} \to \Gamma_{3g}, \Gamma_{4g}$ of MgO: Fe^{2+} at cubic sites. If we assume the absorption coefficient is proportional to the impurity concentration, then we can estimate the corresponding ϵ_2 at 105 cm^{-1} by $\epsilon_2(\omega) = \frac{n\alpha(\omega)}{2\pi\omega}$, where n is the refractive index (for pure MgO, $n \simeq 3.2$ at 105 cm^{-1}), $\alpha(\omega)$ is the absorption coefficient at frequency ω (in units of cm^{-1}). The value of ϵ_2 is about 0.22 for 6% Fe concentration, 0.98 for 27%. As the iron concentration increases, the electronic transitions of Fe^{2+} should show greater influence on the far-infrared spectra of ferropericlase. In our measurement the spectra below 200 cm^{-1} are complicated due to the presence of fringes, consequently we can not confirm this tendency. Henning et $al.$[27] measured the infrared reflectance of Fe$_x$Mg$_{1-x}$O for $x = 1.0$, 0.9, 0.8, 0.7, 0.5 and 0.4 at room temperature. The ϵ_2 curves reported in their paper do not show a monotonic rise in the far-infrared region as the iron concentration x increases from 0.4 to 1.0, while they are all in the range of 6-10 near 100 cm^{-1}. It is difficult to explain such large ϵ_2 with lattice vibrations alone, and the accuracy of these data has been questioned.[28] Further experiments are needed to clarify this issue.

V. CONCLUSIONS

The infrared reflectance spectra of magnesium oxide and ferropericlase has been measured at 295 and 6 K. It is found that ϵ_∞ increases as Fe concentration increases, while the width of the TO modes remains the same in the doped materials. We construct a theoretical model which includes both disorder scattering and anharmonic phonon-phonon interactions. The model shows fairly good agreement with the experiment in the regions where the lowest-order perturbation is relatively large. Near the resonance, theory and experiment both have smaller self-energies, which makes the reflectance quite sensitive to the details. We do not know whether the disagreements with experiment in the region are caused by neglect of higher order corrections, or by inaccuracy of the underlying model. However, the model identifies the global features reasonably well, and may provide a good basis for the study of phonon decay needed for a theory of heat conductivity.

Acknowledgments

---

[*] Electronic address: tsun@grad.physics.sunysb.edu

[1] T. Yagi and N. Funamori, Phil. Trans. **354**, 1711 (1996).

[2] A. M. Hofmeister, Science **283**, 1699 (1999).

[3] A. M. Hofmeister, J. Geodyn. **40**, 51 (2005).

[4] A. F. Goncharov, V. V. Struzhkin, and S. D. Jacobsen, Science **312**, 1205 (2006).

[5] D. M. Sherman, J. Geophys. Res. **96**, 14299 (1991).

[6] J. Badro, G. Fiquet, F. Guyot, J.-P. Rueff, V. V. Struzhkin, G. Vankó, and G. Monaco, Science **300**, 789 (2003).

[7] J.-F. Lin, V. V. Struzhkin, S. D. Jacobsen, M. Y. Hu, P. Chow, J. Kung, H. Liu, H.-K. Mao, and R. J. Hemley, Nature **436**, 377 (2005).

[8] R. G. Burns, *Mineralogical Applications of Crystal Field Theory* (Cambridge Univ. Press, Cambridge, 1993), 2nd ed.

[9] H. Keppler, I. Kantor, and L. S. Dubrovinsky, Am. Mineral. **92**, 433 (2007).

[10] J. R. Jasperse, A. Kahan, and J. N. Plendl, Phys. Rev. **146**, 526 (1966).

[11] S. D. Jacobsen, H. J. Reichmann, H. A. Spetzler, S. J. Mackwell, J. R. Smyth, R. J. Angel, and C. A. McCammon, J. Geophy. Res. **107, No. B2**, ECV 4 (2002).

[12] C. C. Homes, M. Reedyk, D. A. Crandles, and T. Timusk, Appl. Opt. **32**, 2972 (1993).

[13] R. A. Cowley, Rep. Progr. Phys. **31, part 1**, 123 (1968).

[14] G. K. Horton and A. A. Maradudin, eds., *Dynamical Properties of Solids* (North-Holland Publishing Company, 1975), vol. 2, chap. 5.

[15] J. Fabian and P. B. Allen, Phys. Rev. Lett. **77**, 3839 (1996).

[16] J. D. Gale, JCS Faraday Trans. **93**, 629 (1997).

[17] A. M. Stoneham and M. J. L. Sangster, Phil. Mag. B **52**, 717 (1985).

[18] M. J. L. Sangster, J. Phys. Chem. Solids **34**, 355 (1973).

[19] M. J. L. Sangster, G. Peckham, and D. H. Saunderson, J. Phys. C: Solid State Phys. **3**, 1026

(1970).

[20] G. Kugel, C. Carabatos, B. Hennion, B. Prevot, A. Revcolevschi, and D. Tocchetti, Phys. Rev. B **16**, 378 (1977).

[21] M. J. L. Sangster and A. M. Stoneham, Phil. Mag. B **43**, 597 (1981).

[22] E. R. Cowley, J. Phys. C: Solid State Phys. **5**, 1345 (1972).

[23] R. J. Elliott, J. A. Krumhansl, and P. L. Leath, Rev. Mod. Phys. **46**, 465 (1974).

[24] A. D. Bruce, J. Phys. C: Solid State Phys. **6**, 174 (1973).

[25] D. D. S. Meneses, J. Brun, P. Echegut, and P. Simon, Appl. Spectro. **58**, 969 (2004).

[26] J. Y. Wong, Phys. Rev. **168**, 337 (1968).

[27] T. Henning, B. Begemann, H. Mutschke, and J. Dorschner, Astron. Astrophys. Suppl. Ser. **112**, 143 (1995).

[28] A. M. Hofmeister, E. Keppel, and A. K. Speck, Mon. Not. R. Astron. Soc. **345**, 16 (2003).